

Giant room-temperature anomalous terahertz Faraday rotation in the magnetic Weyl semimetal Co_2MnGa

Xingyue Han,¹ Anastasios Markou,² Jonathan Stensberg,¹ Yan Sun,² Claudia Felser,² and Liang Wu^{1,*}

¹*Department of Physics and Astronomy, University of Pennsylvania, Philadelphia, Pennsylvania 19104, USA*

²*Max-Planck-Institut für Chemische Physik fester Stoffe, 01187 Dresden, Germany*

(Dated: December 23, 2021)

We report measurement of terahertz anomalous Hall conductivity and Faraday rotation in the magnetic Weyl semimetal Co_2MnGa thin films as a function of the magnetic field, temperature and thickness, using time-domain terahertz spectroscopy. The terahertz conductivity shows a thickness-independent anomalous Hall conductivity of around $600 \Omega^{-1} \cdot \text{cm}^{-1}$ at room temperature, and it is also frequency-independent from 0.2-1.5 THz. The magnitude of both the longitudinal and Hall conductivity, the weak spin-orbit coupling and the position of Weyl points very close to the chemical potential all satisfy the criteria for intrinsic anomalous Hall conductivity. First-principle calculation also supports the frequency-independent intrinsic anomalous Hall conductivity at low frequency. We also find a thickness-independent Faraday rotation of $59 (\pm 6)$ mrad at room temperature, which comes from the intrinsic Berry curvature contribution. In the thinnest 20 nm sample, the Faraday rotation divided by the sample thickness reaches around 3 mrad/nm due to Berry curvature, and is the largest reported at room temperature. The giant Verdet constant of the order of $10^6 \text{ rad m}^{-1} \text{ T}^{-1}$ at room temperature indicates that Co_2MnGa is of great potential for applications as optical isolator and modulator in the THz spectral range. The Hall angle from 0.2-1.5 THz is around 8.5 % at room temperature, which is promising for THz spintronics.

Introduction

The last decade witnessed an explosion of research on topological states of matter characterized by the topological properties of the bulk wave-functions¹⁻³. Topological insulators are robust to adiabatic perturbation as long as the bulk gap is not closed^{2,3}. Weyl semimetals are newly discovered topological states of matter without a bulk gap and with open Fermi surface arcs when either time-reversal or inversion symmetry is broken⁴⁻¹¹. These materials have accidental band touching at pairs of points with different chirality in the momentum space. Near these points, the quasi-particles (low-energy excitations) can be described by Weyl equations first proposed by Hermann Weyl in 1929¹². As a result, these touching points in the band structure are called Weyl points, and the quasi-particles near them resemble Weyl fermions. The bulk wave functions in Weyl semimetals acquire a Berry phase as they move around the Weyl point because each Weyl node behaves like a fictional magnetic field known as Berry curvature. These Weyl points (monopoles in k space) are also topologically protected because translation-invariant perturbations are identical to moving Weyl points in the momentum space, unless they meet in the zone boundary and annihilate with each other.

Weyl semimetals host many exotic phenomena including interesting temperature and frequency dependence in optical conductivity¹³⁻¹⁵, novel quantum oscillations related with Fermi arcs¹⁶, giant second harmonic generation^{17,18}, as well as a chiral magnetic effect and intrinsic anomalous Hall effect¹⁹. Experimental signatures of Weyl semi-metals are still far behind the advance of various theoretical proposals. Thus far, the widely experimentally studied Weyl semi-metal materials are non-magnetic, but with broken inversion symmetry^{9-11,20}.

Fermi arcs in magnetic $\text{Co}_3\text{Sn}_2\text{S}_2$ and Co_2MnGa were identified recently^{21,22}, which established direct evidence for the magnetic Weyl semimetals. Among them, Co_2MnGa is particularly interesting as it is a room temperature ferromagnetic with a large anomalous Hall effect and a high curie temperature at $T_C=690 \text{ K}$ ^{23,24}. Bulk Co_2MnGa is a Heusler compound, which has a cubic face-centered structure with space group $Fm\bar{3}m$ (No. 225). Large anomalous Nernst effects are also observed in both bulk and thin films²⁵⁻²⁷.

The anomalous Hall effect (AHE) has been studied extensively in conventional ferromagnetic materials^{28,29}. The intrinsic AHE is a scattering-independent process first proposed by Karplus and Luttinger³⁰, which depends only on the topological band structure with the contribution of the Berry curvature in the momentum space^{28,31,32}. The AHE can be greatly enhanced when Fermi energy is close to band (anti-)crossings such as the Weyl points³³⁻³⁵. Due to its exotic band structure, magnetic Weyl semimetals (WSMs) such as Co_2MnGa are a good platform to study the intrinsic AHE^{36,37}. When the chemical potential is close to the Weyl points, the nonzero net Berry curvature effect is dominating, and a large intrinsic anomalous Hall effect can be calculated by the Kubo formula and compared with experiments²⁸.

Another advantage of Co_2MnGa is that thin films, which are ideal for device applications, can be fabricated by sputtering. The samples studied in this work are grown by sputtering on MgO substrates and capped with 3 nm Al, the growth details of which were the subject of previous study²⁴. At room temperature, transport measurement on thin films show a large anomalous Hall conductivity (AHC) of $814 \Omega^{-1} \cdot \text{cm}^{-1}$ and a large anomalous Hall angle (AHA) of 10.5 %²⁴. However, the spectrum of the anomalous Hall conductivity, $\sigma_{xy}(\omega)$, and Hall an-

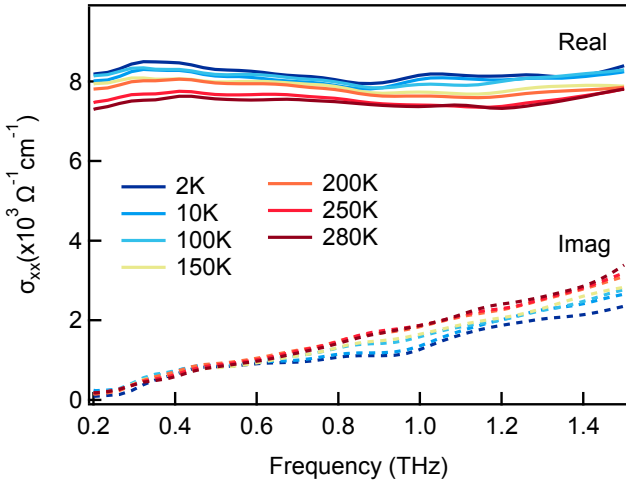


FIG. 1. Longitudinal conductivity spectra $\sigma_{xx}(\omega)$ of a 40 nm Co_2MnGa thin film from 2 K to 280 K. The solid lines are the real part. The dashed lines are the imaginary part.

gle, $\theta_H(\omega)$, at terahertz frequency remain missing. Future high-speed spintronic devices will crucially rely on such AHE phenomena at terahertz (THz) frequencies. Current DC AHE transport measurements significantly lag behind other interests of information carriers such as electrons in field-effect transistors featuring cut-off frequencies of around 1 THz³⁸. Therefore, a proper understanding of the thin-film properties at THz frequencies is required. Another intriguing aspect is the possibly giant magneto-optical Faraday effect, i.e. the rotation of the light polarization of the transmitted light for the magnetic media, resulting from the enhanced Hall conductivity on the transitions near the Weyl point. The magnitude of the Faraday rotation is proportional to the terahertz Hall conductivity. This novel optical property inherent to the magnetic WSM remains to be explored.

In our work, we study the THz AHC, AHA and Faraday rotation spectra of Co_2MnGa thin films using magneto-optical methods. We employ time-domain terahertz spectroscopy (TDTS) to measure optical longitudinal conductivity and complex Faraday rotation at 0.2–1.5 THz. Giant THz AHC and AHA at RT around $600 \Omega^{-1} \cdot \text{cm}^{-1}$ and 8.5 % are observed. AHE remains operative from DC up to 1.5 THz with a flat frequency response in thin films. The optical Faraday rotation and AHC both show a thickness-independent behavior at RT. One of the samples exhibits a 2.5 mrad/nm Faraday rotation divided by thickness, which is the largest value reported at RT. Using first-principle calculation, we show that the AHC and Faraday rotation are dominating from the intrinsic contribution.

Results and Discussion

We present the zero-field terahertz conductivity on these films first. Utilizing TDTS, we obtain the complex longitudinal conductivity spectra, $\sigma_{xx}(\omega)$, as we measure

both the amplitude and the phase of the transmission without using Kramers–Kronig transformation^{39,40}. In the thin-film approximation, the longitudinal conductivity can be extracted from the following relation:

$$T_{xx}(\omega) = \frac{n+1}{n+1+d\sigma_{xx}(\omega)Z_0} \exp\left(i\frac{\omega}{c}\Delta L(n-1)\right). \quad (1)$$

Here T_{xx} is the transmission coefficient of the thin film, n is the refractive index of the substrate, d is the thickness of the film, Z_0 is the impedance of free space, ΔL is the thickness mismatch between the sample and the bare substrate. Fig. 1 shows the real and imaginary part of $\sigma_{xx}(\omega)$ of 40 nm Co_2MnGa from 2 K to 280 K. The temperature dependence is quite weak as the the real conductivity changes only by 8 % from 2 K to 280 K. The results follow the Drude model, $\sigma_{xx}(\omega) = \sigma_0/(1-i\omega\tau) - i\epsilon_0(\epsilon_\infty - 1)\omega$, where σ_0 is the DC conductivity, τ is the scattering time, ϵ_0 is the vacuum permittivity, and ϵ_∞ is a constant that describes lattice polarizability at high frequency. The flat spectra in the real part (solid lines) and the small linear spectra of $\text{Im } \sigma_{xx}(\omega)$ (dashed lines) both indicates a short τ . Fitting shows $1/\tau$ is around 3–5 THz in the whole temperature range. The magnitude of the real part of the longitudinal conductivity falls into one of the criteria for intrinsic AHE^{41,42} as discussed below.

Besides the intrinsic contribution to AHE, there are two other kinds of extrinsic contributions: skew scattering and side jump²⁸. In ferromagnets, the combination of the total anomalous Hall and longitudinal conductivity show a crossover behavior in three regions according to the magnitude of longitudinal conductivity^{41,42}: dirty regime ($\sigma_{xx} < 10^4 \Omega^{-1} \cdot \text{cm}^{-1}$), intermediate regime ($\sigma_{xx} = 10^4 - 10^6 \Omega^{-1} \cdot \text{cm}^{-1}$), and extreme conducting regime ($\sigma_{xx} > 10^6 \Omega^{-1} \cdot \text{cm}^{-1}$). The intrinsic contribution always dominates in the intermediate regime. The magnitude of the real part of the longitudinal conductivity in Co_2MnGa falls at the lower boundary in the intermediate regime. Often, to separate the three contributions, the scaling relation between longitudinal conductivity and anomalous Hall conductivity is used. The contribution of the skew scattering to the AHC is proportional to the square of longitudinal conductivity $\sigma_{xy}^{A-\text{skew}} \propto \sigma_{xx}^2$, while the intrinsic and side-jump contributions are both independent of the longitudinal conductivity. Previous DC transport on Co_2MnGa bulk crystal used the scaling relation and revealed that the intrinsic AHC is around $10^3 \Omega^{-1} \cdot \text{cm}^{-1}$ ^{21,23}.

Nevertheless, it is very difficult to separate the intrinsic contribution and side jump in DC transport²⁸. Interestingly, Co_2MnGa also satisfies the other two criteria that favors intrinsic contribution⁴². 1) The AHC is on the order of $1000 \Omega^{-1} \cdot \text{cm}^{-1}$. The intrinsic AHC value in the thin film and bulk crystal was reported to be $1138 \Omega^{-1} \cdot \text{cm}^{-1}$ ²⁴ and $1164 \Omega^{-1} \cdot \text{cm}^{-1}$ ²³ respectively. 2) The anticrossing point (the Weyl point) is only around 80 meV above the chemical potential²¹. Because of these three criteria, one can perform first-principles calculations to

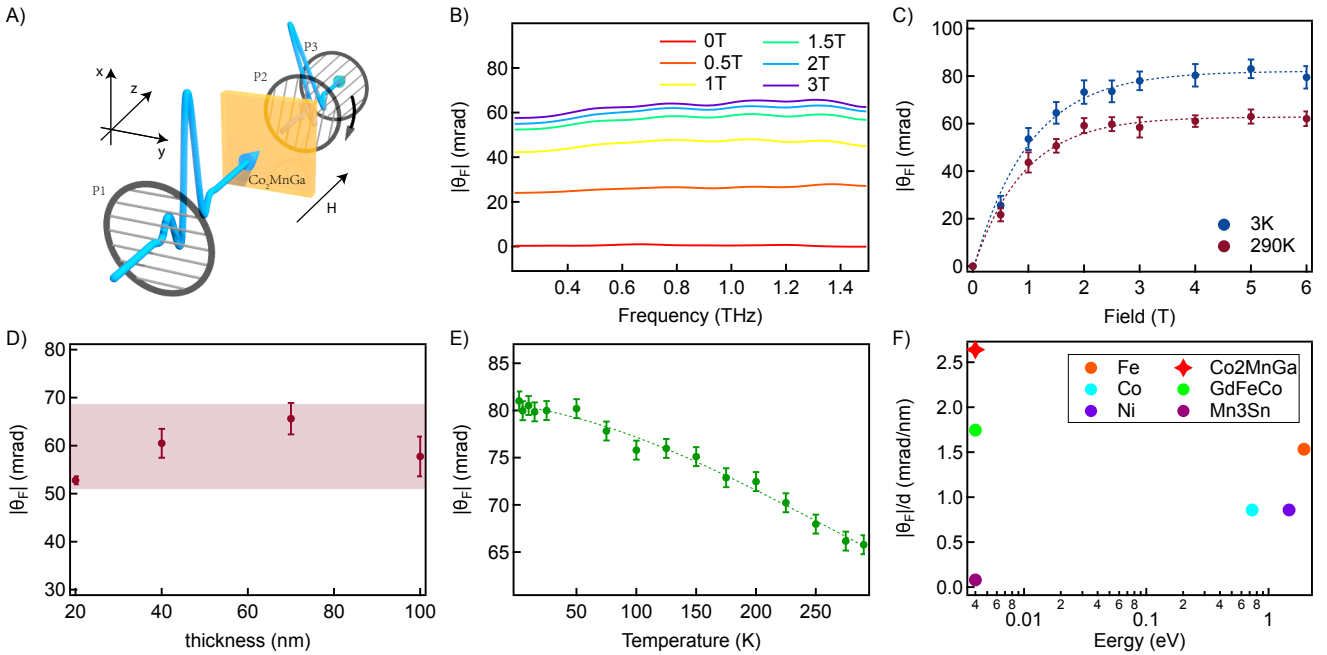


FIG. 2. A) A sketch of the experimental geometry of the Faraday rotation measurement. B) Field dependent Faraday angle spectra of a 40 nm Co₂MnGa sample at 290 K. C) Field dependence of the average Faraday angle over the frequency range of 0.2-1.5 THz of the 40 nm Co₂MnGa sample. D) Thickness independent Faraday angle under 2 T at 290 K. E) Temperature dependence of Faraday angle of the 40 nm Co₂MnGa under 2.5 T. F) Thickness normalized Faraday rotation of several ferromagnets at RT.

reliably predict the frequency-dependent intrinsic contribution and compare it with experiments.

With a set of freestanding wire-grid polarizers as shown in Fig. 2A, our TDTS can resolve the polarization state of the THz signal and measure the frequency dependent AHC. Three THz wire-grid polarizers (P1,P2,P3, extinction ratio>2000 at 1 THz) are used to measure the Faraday angle. P1 aligns the incident polarization vertically. P2 is mounted on a rotation stage (not shown in the figure) to selectively pass the vertical electric field (E_x) or horizontal electric field (E_y). P3 is fixed at 45° so that E_x and E_y have the same response at the detector. The polarization change before and after the Co₂MnGa film is the Faraday rotation $\theta_F(\omega) = \frac{E_y(\omega)}{E_x(\omega)}$.

These measurements were performed under an out-of-plane magnetic field up to 7 T. To exclude the nonmagnetic effects such as birefringence from the windows, we apply $\pm B$ to get a symmetrized Faraday angle spectra $\theta_F(\omega, H) = [\theta_F^{meas}(\omega, H) - \theta_F^{meas}(\omega, -H)]/2$. Fig. 2B shows the Faraday angle $\theta_F(\omega)$ of the 40 nm sample at 290 K. The rotation has a weak dependence on the frequency. The field dependence is similar to the known magnetization curve with a saturation field $H_s \approx 1.5$ T²⁴ as shown in Fig. 2C. Note that usually the Faraday rotation is proportional to the thickness and characterized by the Verdet constant⁴³. The large θ_F around 60 mrad at room temperature is nearly thickness independent as in Fig. 2D, which mainly contribute from the

anomalous terahertz Hall effect. θ_F increases monotonically and reaches 80 mrad as the temperature cools down to 2K (see Fig. 2E). Below 1 Tesla, the Verdet constant of the 40 nm sample reaches $10^6 \text{ rad m}^{-1} \text{T}^{-1}$, which is of similar size of the giant magneto-optical effect in topological insulators HgTe⁴⁴ and Bi₂Se₃^{40,45} at low temperature. In Fig. 2F, we show the normalized Faraday rotation by thickness at room temperature, Co₂MnGa has the largest value of 3 mrad/nm to our best knowledge. It is 30 times larger than the value in the Weyl antiferromagnet candidate Mn₃Sn^{46,47}. Even if we compare it with other reported values at low temperature, 3 mrad/nm is larger than any material report and is similar to another magnetic Weyl semimetal Co₃Sn₂S₂⁴⁸.

The terahertz Hall conductivity spectra $\sigma_{xy}(\omega)$ can be extracted from the Faraday rotation by the relation $\sigma_{xy}(\omega) = \theta_F(\sigma_{xx} + \frac{n+1}{dZ_0})$, where n is the refractive index of the substrate, Z_0 is the vacuum impedance and d is the thickness of the film. FIG. 3A shows the terahertz Hall conductivity $\sigma_{xy}(\omega)$ of 40 nm Co₂MnGa. Consistent with the flat spectra of longitudinal conductivity and Faraday rotation, it is also independent of frequency. The mean value between 0.2 and 1.5 THz under each field is plotted in FIG. 3B, again scaling with the magnetization²⁴. According to the Hall conductivity formula:

$$\sigma_{xy} = R_0 H + \sigma_{xy}^A \quad (2)$$

The total Hall conductivity $\sigma_{xy}(\omega)$ consists of the or-

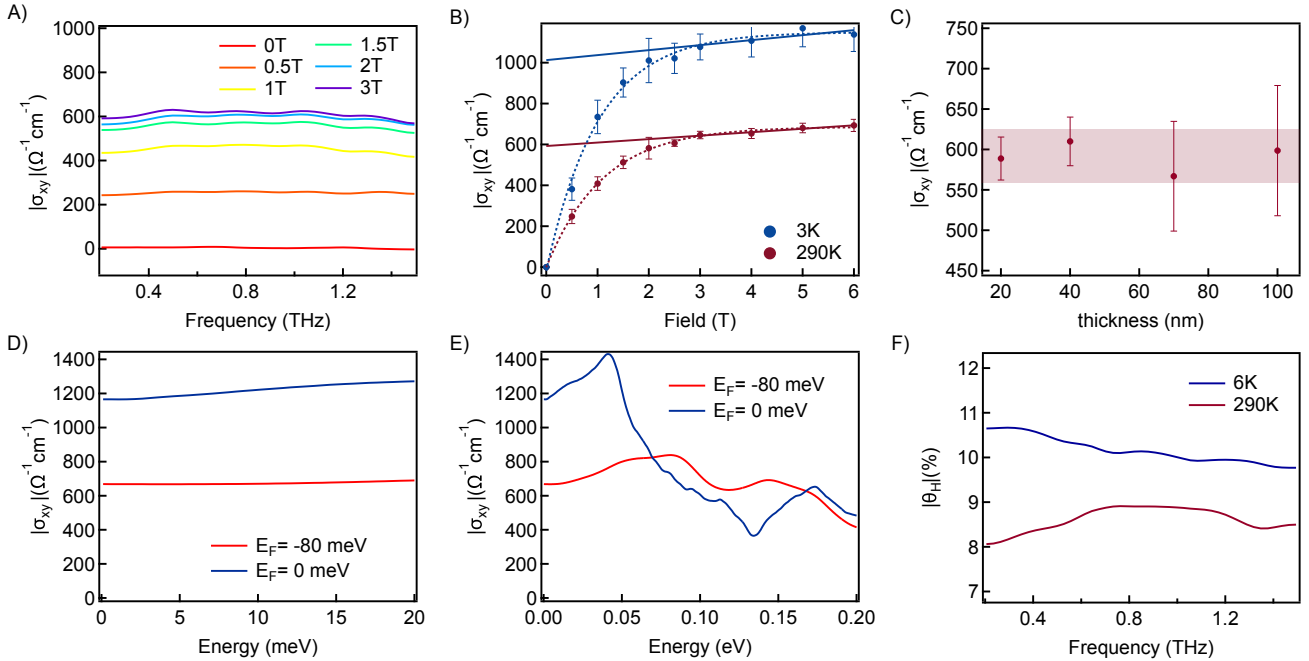


FIG. 3. A) Field dependent Hall conductivity spectra of the 40 nm Co₂MnGa at 290 K. B) Field dependence of the average Hall conductivity over frequency range of 0.2-1.5 THz of the 40nm Co₂MnGa at 3 K and 290 K. The intercepts of dashed lines on the vertical axis are the anomalous Hall conductivity σ_{xy}^A . C) Thickness independent Hall conductivity σ_{xy} under 2 T at 290 K. D,E) First principle calculation of RT Hall conductivity with $E_F = -80$ meV and 0 meV. We define the Weyl point position as 0 meV. F) Hall angle spectra of the 40 nm Co₂MnGa at 6 K and 290 K

inary Hall effect, $R_0 H$, where R_0 is the ordinary Hall coefficient, and the anomalous Hall effect, σ_{xy}^A . The ordinary Hall conductivity scales with the magnetic field. The anomalous term can be obtained by extrapolating the high field data to zero field (FIG. 3B intersection). The 40 nm Co₂MnGa shows a giant value of $|\sigma_{xy}^A| = 930 \Omega^{-1} \cdot \text{cm}^{-1}$ at 2 K, and $|\sigma_{xy}^A| = 590 \Omega^{-1} \cdot \text{cm}^{-1}$ at 290 K. These results are consistent with the DC transport values on the 40 nm Co₂MnGa²⁴. Similar to RT Faraday rotation, the RT Hall effect is also thickness independent, with the Hall conductivity value around $600 \Omega^{-1} \cdot \text{cm}^{-1}$ as shown in FIG. 3C. We would like to point out that substrates from different vendors and different capping could lead to a change of 10% of AHC at room temperature. Note that the experiment value $|\sigma_{xy}^{exp}| \sim 600 \Omega^{-1} \cdot \text{cm}^{-1}$ is very close to the theoretical prediction of intrinsic Hall effect in the order of $|\sigma_{xy}^{int}| \sim e^2/ha \sim 670 \Omega^{-1} \cdot \text{cm}^{-1}$ for Co₂MnGa⁴¹, where a is the lattice constant. This indicates that the intrinsic contribution (the Berry curvature) is the leading effect.

The large scattering rate in Co₂MnGa makes it difficult to separate the intrinsic and side jump contributions via the scaling of σ_{xy} versus σ_{xx}^2 at terahertz frequency, as the measured THz frequency range is comparable to the scattering rate²⁸. Nevertheless, as we discussed above, because Co₂MnGa satisfies the three criteria for intrinsic anomalous Hall conductivity in terms of longitudinal conductivity, Hall conductivity, and chem-

ical potential, it is quite accurate to use density functional theory (DFT) to calculate and identify the intrinsic contribution. We calculate the electronic band structure based on DFT by employing the full-potential local-orbital code (FPLO) with localized atomic basis⁴⁹. The exchange and correlation energies were considered in the generalized gradient approximation (GGA) level following the Perdew–Burke–Ernzerhof parametrization scheme⁵⁰. Following experimental results, we set a ferromagnetic structure with magnetic moment along z direction²³. We projected the Bloch wavefunction into high symmetric atomic-orbital-like Wannier functions and constructed the tight-binding model Hamiltonian by the Wannier function overlap. Based on the tight-binding model Hamiltonian, the DC anomalous Hall conductivity and THz conductivity were computed by following the Kubo formula approach in linear response approximation and clean limit^{31,52–54}, with AHC

$$\sigma_{xy}^{DC}(E_F) = 2e^2 \hbar \int_{BZ} \frac{d^3k}{(2\pi)^3} \sum_{E_n(k) \leq E_F} f_n(k) \quad (3)$$

$$Im \sum_{m \neq n} \frac{< u_n(k) | \hat{v}_x | u_m(k) > < u_m(k) | \hat{v}_y | u_n(k) >}{(E_m(k) - E_n(k))^2 + \eta^2}$$

and terahertz conductivity

$$\sigma_{xy}(\hbar\omega) = ie^2\hbar \int_{BZ} \frac{d^3k}{(2\pi)^3} \sum_{m \neq n} \frac{f_m(k) - f_n(k)}{E_m(k) - E_n(k)} \frac{\langle u_n(k) | \hat{v}_x | u_m(k) \rangle \langle u_m(k) | \hat{v}_y | u_n(k) \rangle}{E_m(k) - E_n(k) - (\hbar\omega + i\eta)} \quad (4)$$

where $f_n(k)$ is the Fermi-Dirac distribution, $E_n(k)$ is the eigenvalue of n th band with eigenstate $|u_n(k)\rangle$, $\hat{v}_x(k) = \frac{1}{\hbar} \frac{\partial \hat{H}(k)}{\partial k_x}$ is the velocity operator, $\hbar\omega$ is the transition energy, and η is a smearing parameter to avoid numerical divergence. (Here we set $\eta=0.1$ meV.) We used a dense k -grid of 240^3 for the numerical integration. As shown in FIG. 3D, when the Weyl points are around 80 meV above the chemical potential, it matches the anomalous THz Hall conductivity, which also agrees with previous transport and ARPES studies^{21,24}. FIG. 3D shows the intrinsic anomalous THz Hall conductivity over a larger frequency range with resonant features associated with Berry curvature contribution, which we hope future experiments could explore.

We also measure the Hall angle at THz frequency,

$\theta_H = \frac{\sigma_{xy}(\omega)}{\sigma_{xx}(\omega)}$, as it will be useful for field-effect transistors around 1 THz³⁸. A large Hall angle $\sim 8.5\%$ is observed at 290 K, as shown in FIG. 3F. It increases as temperature decreases and reaches a maximum with 10 % at 2 K. Co₂MnGa is one of few materials that exhibits large AHE and large Hall angle at the same time. Since AHE and spin Hall effect are generated by the same mechanisms, the large AHE in Co₂MnGa guarantees a large spin Hall effect, which was reported recently⁵⁵. Looking forward, we believe that our observation of large THz anomalous Hall conductivity, Faraday rotation, and Hall angle from the intrinsic contribution at room temperature will be critical to use Co₂MnGa for future applications such as optical isolator, modulator, and topological spintronics at the THz frequencies.

X.H., J.S. and L.W. acknowledge the support from the ARO under the Grants W911NF1910342 and W911NF2020166. X.H. and J.S. are also partially supported by the Gordon and Betty Moore Foundation's EPiQS Initiative, Grant GBMF9212 to L.W. The acquisition of the laser for the THz system is support from a seed grant at National Science Foundation supported University of Pennsylvania Materials Research Science and Engineering Center (MRSEC)(DMR-1720530).

* liangwu@sas.upenn.edu

- ¹ J. E. Moore, *Nature* **464**, 194 (2010).
- ² M. Z. Hasan and C. L. Kane, *Rev. Mod. Phys.* **82**, 3045 (2010).
- ³ X.-L. Qi and S.-C. Zhang, *Rev. Mod. Phys.* **83**, 1057 (2011).
- ⁴ X. Wan, A. M. Turner, A. Vishwanath, and S. Y. Savrasov, *Physical Review B* **83**, 205101 (2011).
- ⁵ A. Burkov and L. Balents, *Physical Review Letters* **107**, 127205 (2011).
- ⁶ G. Xu, H. Weng, Z. Wang, X. Dai, and Z. Fang, *Physical Review Letters* **107**, 186806 (2011).
- ⁷ H. Weng, C. Fang, Z. Fang, B. A. Bernevig, and X. Dai, *Physical Review X* **5**, 011029 (2015).
- ⁸ S.-M. Huang, S.-Y. Xu, I. Belopolski, C.-C. Lee, G. Chang, B. Wang, N. Alidoust, G. Bian, M. Neupane, C. Zhang, *et al.*, *Nature Communications* **6** (2015).
- ⁹ S.-Y. Xu, I. Belopolski, N. Alidoust, M. Neupane, G. Bian, C. Zhang, R. Sankar, G. Chang, Z. Yuan, C.-C. Lee, *et al.*, *Science* **349**, 613 (2015).
- ¹⁰ B. Lv, H. Weng, B. Fu, X. Wang, H. Miao, J. Ma, P. Richard, X. Huang, L. Zhao, G. Chen, *et al.*, *Physical Review X* **5**, 031013 (2015).
- ¹¹ L. Yang, Z. Liu, Y. Sun, H. Peng, H. Yang, T. Zhang, B. Zhou, Y. Zhang, Y. Guo, M. Rahn, *et al.*, *Nature Physics* **11**, 728 (2015).
- ¹² H. Weyl, *Zeitschrift für Physik A Hadrons and Nuclei* **56**, 330 (1929).
- ¹³ P. Hosur, S. Parameswaran, and A. Vishwanath, *Physical review letters* **108**, 046602 (2012).
- ¹⁴ B. Xu, Z. Fang, M.-Á. Sánchez-Martínez, J. W. Venderbos, Z. Ni, T. Qiu, K. Manna, K. Wang, J. Paglione, C. Bernhard, *et al.*, *Proceedings of the National Academy of Sciences* **117**, 27104 (2020).
- ¹⁵ Z. Ni, B. Xu, M.-Á. Sánchez-Martínez, Y. Zhang, K. Manna, C. Bernhard, J. Venderbos, F. de Juan, C. Felser, A. G. Grushin, *et al.*, *npj Quantum Materials* **5**, 1 (2020).
- ¹⁶ A. C. Potter, I. Kimchi, and A. Vishwanath, *Nature communications* **5** (2014).
- ¹⁷ L. Wu, S. Patankar, T. Morimoto, N. L. Nair, E. Thewalt, A. Little, J. G. Analytis, J. E. Moore, and J. Orenstein, *Nature Physics* **13**, 350 (2017).
- ¹⁸ S. Patankar, L. Wu, B. Lu, M. Rai, J. D. Tran, T. Morimoto, D. E. Parker, A. G. Grushin, N. Nair, J. Analytis, *et al.*, *Physical Review B* **98**, 165113 (2018).
- ¹⁹ A. Burkov, *Journal of Physics: Condensed Matter* **27**, 113201 (2015).
- ²⁰ L. Wu, S. Patankar, T. Morimoto, N. L. Nair, E. Thewalt, A. Little, J. G. Analytis, J. E. Moore, and J. Orenstein, *Nature Physics* **13**, 350 (2017).
- ²¹ I. Belopolski, K. Manna, D. S. Sanchez, G. Chang, B. Ernst, J. Yin, S. S. Zhang, T. Cochran, N. Shumiya, H. Zheng, *et al.*, *Science* **365**, 1278 (2019).
- ²² N. Morali, R. Batabyal, P. K. Nag, E. Liu, Q. Xu, Y. Sun, B. Yan, C. Felser, N. Avraham, and H. Beidenkopf, *Science* **365**, 1286 (2019).
- ²³ K. Manna, L. Muechler, T.-H. Kao, R. Stinshoff, Y. Zhang, J. Gooth, N. Kumar, G. Kreiner, K. Koepernik, R. Car, J. Kübler, G. H. Fecher, C. Shekhar, Y. Sun, and C. Felser, *Phys. Rev. X* **8**, 041045 (2018).
- ²⁴ A. Markou, D. Kriegner, J. Gayles, L. Zhang, Y.-C. Chen,

B. Ernst, Y.-H. Lai, W. Schnelle, Y.-H. Chu, Y. Sun, and C. Felser, *Phys. Rev. B* **100**, 054422 (2019).

²⁵ A. Sakai, Y. P. Mizuta, A. A. Nugroho, R. Sihombing, T. Koretsune, M.-T. Suzuki, N. Takemori, R. Ishii, D. Nishio-Hamane, R. Arita, *et al.*, *Nature Physics* **14**, 1119 (2018).

²⁶ H. Reichlova, R. Schlitz, S. Beckert, P. Swekis, A. Markou, Y.-C. Chen, D. Kriegner, S. Fabretti, G. Hyeon Park, A. Niemann, *et al.*, *Applied Physics Letters* **113**, 212405 (2018).

²⁷ G.-H. Park, H. Reichlova, R. Schlitz, M. Lammel, A. Markou, P. Swekis, P. Ritzinger, D. Kriegner, J. Noky, J. Gayles, *et al.*, *Physical Review B* **101**, 060406 (2020).

²⁸ N. Nagaosa, J. Sinova, S. Onoda, A. H. MacDonald, and N. P. Ong, *Rev. Mod. Phys.* **82**, 1539 (2010).

²⁹ W.-L. Lee, S. Watauchi, V. Miller, R. Cava, and N. Ong, *Science* **303**, 1647 (2004).

³⁰ R. Karplus and J. Luttinger, *Physical Review* **95**, 1154 (1954).

³¹ D. Xiao, M.-C. Chang, and Q. Niu, *Reviews of modern physics* **82**, 1959 (2010).

³² N. Armitage, E. Mele, and A. Vishwanath, *Reviews of Modern Physics* **90**, 015001 (2018).

³³ Z. Fang, N. Nagaosa, K. S. Takahashi, A. Asamitsu, R. Mathieu, T. Ogasawara, H. Yamada, M. Kawasaki, Y. Tokura, and K. Terakura, *Science* **302**, 92 (2003).

³⁴ Y. Yao, L. Kleinman, A. MacDonald, J. Sinova, T. Jungwirth, D.-s. Wang, E. Wang, and Q. Niu, *Physical review letters* **92**, 037204 (2004).

³⁵ J. Kübler and C. Felser, *EPL (Europhysics Letters)* **114**, 47005 (2016).

³⁶ B. Yan and C. Felser, *Annual Review of Condensed Matter Physics* **8**, 337 (2017).

³⁷ P. Hosur and X. Qi, *Comptes Rendus Physique* **14**, 857 (2013).

³⁸ J. A. Del Alamo, *Nature* **479**, 317 (2011).

³⁹ L. Wu, M. Brahlek, R. V. Aguilar, A. V. Stier, C. M. Morris, Y. Lubashevsky, L. S. Bilbro, N. Bansal, S. Oh, and N. P. Armitage, *Nature Physics* **9**, 410 (2013).

⁴⁰ L. Wu, W.-K. Tse, M. Brahlek, C. M. Morris, R. V. Aguilar, N. Koirala, S. Oh, and N. P. Armitage, *Physical Review Letters* **115**, 217602 (2015).

⁴¹ T. Miyasato, N. Abe, T. Fujii, A. Asamitsu, S. Onoda, Y. Onose, N. Nagaosa, and Y. Tokura, *Physical review letters* **99**, 086602 (2007).

⁴² S. Onoda, N. Sugimoto, and N. Nagaosa, *Physical review letters* **97**, 126602 (2006).

⁴³ R. A. Meyers *et al.*, *Encyclopedia of physical science and technology* (Academic Press, 1987).

⁴⁴ A. Shubaev, G. Astakhov, A. Pimenov, C. Brüne, H. Buhmann, and L. Molenkamp, *Physical review letters* **106**, 107404 (2011).

⁴⁵ R. Valdés Aguilar, A. V. Stier, W. Liu, L. S. Bilbro, D. K. George, N. Bansal, L. Wu, J. Cerne, A. G. Markelz, S. Oh, and N. P. Armitage, *Phys. Rev. Lett.* **108**, 087403 (2012).

⁴⁶ T. Matsuda, N. Kanda, T. Higo, N. Armitage, S. Nakatsuji, and R. Matsunaga, *Nature communications* **11**, 1 (2020).

⁴⁷ D. Khadka, T. R. Thapaliya, S. H. Parra, X. Han, J. Wen, R. F. Need, P. Khanal, W. Wang, J. Zang, J. M. Kikkawa, L. Wu, and S. X. Huang, *Science Advances* **6**, eabc1977 (2020).

⁴⁸ Y. Okamura, S. Minami, Y. Kato, Y. Fujishiro, Y. Kaneko, J. Ikeda, J. Muramoto, R. Kaneko, K. Ueda, V. Kocsis, *et al.*, *Nature communications* **11**, 1 (2020).

⁴⁹ K. Koepernik and H. Eschrig, *Phys. Rev. B* **59**, 1743 (1999).

⁵⁰ J. P. Perdew, K. Burke, and M. Ernzerhof, *Phys. Rev. Lett.* **77**, 3865 (1996).

⁵¹ K. Koepernik, O. Janson, Y. Sun, and J. Brink, *arXiv preprint arXiv:2111.09652* (2021).

⁵² R. Kubo, *Journal of the Physical Society of Japan* **12**, 570 (1957).

⁵³ D. Greenwood, *Proceedings of the Physical Society (1958-1967)* **71**, 585 (1958).

⁵⁴ Nagaosa, Naoto and Sinova, Jairo and Onoda, Shigeki and MacDonald, Allan H and Ong, Nai Phuan, *Reviews of modern physics* **82**, 1539 (2010).

⁵⁵ L. Leiva, S. Granville, Y. Zhang, S. Dushenko, E. Shigematsu, T. Shinjo, R. Ohshima, Y. Ando, and M. Shiraishi, *Physical Review B* **103**, L041114 (2021).